# A Method to Directly Compute Synchronverter Parameters for Desired Dynamic Response

Shuan Dong, *Student Member, IEEE*, and Yu Christine Chen, *Member, IEEE*

***Abstract*—This paper proposes a method to directly compute controller parameter values in a synchronverter augmented with a so-called damping correction loop, and in so doing, achieve desired transient and steady-state response. The proposed approach is grounded in a reduced third-order system model that captures pertinent dynamic characteristics of the synchronverter active-power loop (APL), particularly those of the dominant mode. This reduced-order model helps to identify and explain a shortcoming in a previous parameter tuning method. Central to the proposed parameter computation method is to express APL parameters of the original system as closed-form functions of the poles of the reduced-order system. Since the reduced-order model retains dominant-mode dynamic behaviours of the original system, APL parameters can be directly computed according to specified APL dominant mode. Time-domain simulations are provided to validate the accuracy of the reduced-order model and the proposed direct-computation parameter tuning method.**

***Index Terms*—Damping correction loop, parameter tuning, synchronverter, virtual synchronous generator.**

## I. Introduction

MOTIVATED by the shift toward environmentally friendly electricity generation, fossil fuel-based generators are expected to be gradually displaced by renewable energy sources (RESs), such as wind and solar. However, due to the way in which RESs are integrated into the grid, high penetration levels pose numerous technical challenges to existing grid operations. For example, since RESs interface with the AC network via power-electronic devices, such as voltage source converters (VSCs), they provide power without contributing inertia to the system. This results in larger frequency deviations and rates of change of frequency following a disturbance [1]. To tackle this, the virtual synchronous generator (VSG) concept [2]–[17] provides a method for mimicking the effect of inertia support using power-electronic devices. Among numerous VSG realizations, the synchronverter is a representative controller design that embeds the mathematical model of a synchronous generator (SG) into the power-electronic converter. In this way, the synchronverter enforces the behaviour of conventional SGs in these converters, and in turn they provide virtual inertia to the grid [2], [6], [10]. Moreover, normal operation of the synchronverter does not depend on phase-locked loops (PLLs) that are used in conventional VSC control strategies, which can cause instability under weak grid conditions [18]. Consequently, the use of synchronverters bypasses PLL-related instabilities when integrating RESs, which are often located in remote areas and connected to weak grids. Another important advantage of the synchronverter is that it realizes frequency and voltage droop controls via its active- and reactive-power loops, respectively [2].

Although the synchronverter, as it was originally described in [2], provides inertia support and operates well in weakly-connected networks, its response speed cannot be adjusted freely without affecting the steady-state frequency droop characteristic. This limits the ability for the synchronverter to achieve fast maximum power-point tracking and to provide timely frequency regulation. To overcome this defect, our previous work in [6] augments the original synchronverter design with the *damping correction loop*, which adjusts the active-power loop (APL) response speed freely without violating the frequency-droop regulation requirement. An important problem that arises from [6] is the need for an accurate and efficient method to tune relevant controller parameters. In this paper, we propose a direct computation method to obtain APL parameter values based on desired transient and steady-state behaviours. Since the proposed method avoids repeated computation of system eigenvalues, bypasses onerous trial-and-error tuning, and simplifies the tuning process, it represents significant improvement over [6].

Relevant VSG parameter tuning methods can be roughly categorized into offline approaches, which tune parameters prior to online operation, and online ones, in which parameters are adjusted in real time during online operation. Among offline approaches [2]–[10], parameters are tuned based on either empirical formulas ([2]), or small-signal analysis with the linearized system transfer function ([3]–[5]) or state-space model ([6]–[10]). Empirical formulas used in [2] do not precisely place the APL dominant poles, so they are unable to tune parameters to achieve the exact desired time-domain transient behaviour. The methods in [3] and [4] (which use transfer-function-based models) neglect the effects of low-pass filters (LPFs) that smooth out measured signals, which may cause inaccurate parameters. Though the method in [5], which is also based on transfer-function analysis, accounts for the LPFs, potentially tedious trial-and-error work is needed during the tuning process. This is also true for the methods in [6]–[8], which tune parameters based on eigenvalues of the linearized system state-space model. The method in [9] tunes parameters using eigenvalue parametric sensitivities rather than through trial-and-error, but it aims only to stabilize the system instead of achieving exact pole placement. While the method in [10] places poles at prescribed locations, the solution to a computationally burdensome nonlinear optimization problem is required to obtain parameter values. Among online approaches, [11] tunes parameters using the linearized system

S. Dong and Y. C. Chen are with the Department of Electrical and Computer Engineering at The University of British Columbia, Vancouver, BC, V6T 1Z4, Canada. Email: {shuan, chen}@ece.ubc.ca.

transfer function without considering LPFs, and thus may result in inaccurate parameters, as in [3] and [4]; [12] runs a self-tuning algorithm and searches for parameter values for the VSG during online operation, which adds nontrivial computational burden. In this paper, we propose an accurate parameter tuning method for the synchronverter augmented with the damping correction loop. Unlike previous approaches, the proposed method accounts for LPFs for measured signals, avoids trial-and-error procedures, and achieves precise pole placement with little computational burden.

Contributions of this paper are as follows. First, we identify a shortcoming in a previous parameter tuning method for the synchronverter augmented with the damping correction loop from [6]. Particularly, we reveal that during the parameter tuning process, changing the same parameter influences system eigenvalues differently under various operating conditions. Analytical justification for this phenomenon is provided using root locus analysis for the characteristic equation of a reduced-order model. Through this analysis, we develop a precise criterion to predict different eigenvalue variation patterns. Thereafter, we bypass this uncertainty in the parameter tuning process and propose a direct computation method, which obtains the synchronverter APL parameters according to prescribed pole locations. Since the proposed method relies on the exact solution of a set of three algebraic equations, it ensures parameter accuracy while being computationally tractable. Finally, we validate the accuracy of the proposed criterion and the direct computation method via numerical case studies. It is worth noting that, in this paper, we include the LPFs in the reduced-order APL model (unlike in [6]), which improves the model accuracy and allows us to compute APL parameters in analytical closed form given desired dynamic response.

The remainder of this paper is organized as follows. Section II provides an overview of the synchronverter augmented with the damping correction loop and identifies a shortcoming in tuning its parameters with small-signal analysis. In Section III, we develop and adopt a criterion to explain the highlighted shortcoming, and we further propose the direct parameter computation method. Through extensive case studies, Section IV validates the proposed criterion and the direct computation method. Finally, Section V provides concluding remarks and directions for future research.

## II. Preliminaries

The synchronverter comprises active- and reactive-power loops, which regulate the synchronverter active- and reactive-power outputs, respectively. Our previous work in [6] appends the damping correction loop (see Fig. 1) to the synchronverter APL so that its response speed can be adjusted without violating the frequency regulation requirement. To tune APL parameters, [6] adopts an iterative method based on small-signal analysis, in which system eigenvalues are checked repeatedly with different parameter values in an effort to place the APL dominant poles at desired locations. However, we find that the damping correction loop parameter influences the APL dominant mode differently under different conditions, which introduces uncertainty to the iterative tuning process

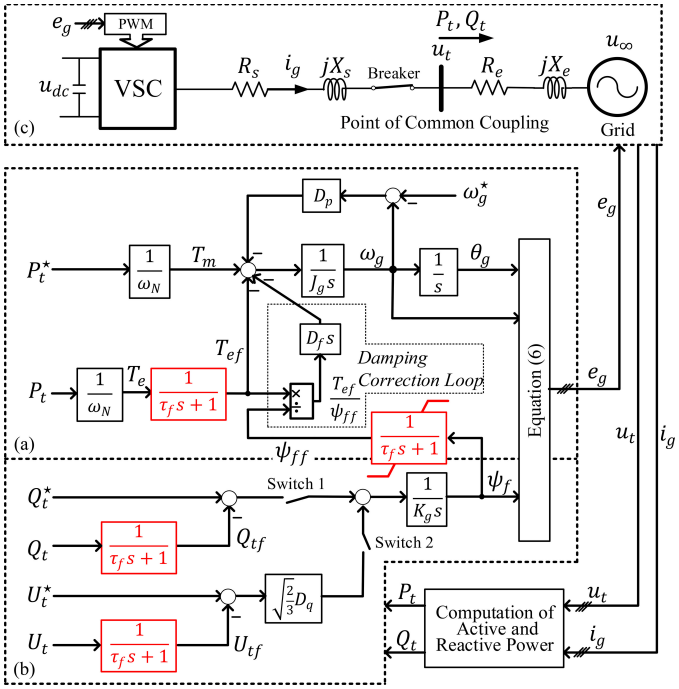


Fig. 1. Synchronverter augmented with damping correction loop [6]. In [6], parameters are tuned via an iterative method, which requires repeated computation of system eigenvalues and onerous trial-and-error effort. The parameter tuning method proposed in this paper avoids these shortcomings.

proposed in [6]. In this section, we provide an overview of the synchronverter with the damping correction loop and motivate the need to improve the parameter tuning method in [6].

### A. Synchronverter with Damping Correction Loop [6]

As shown in Fig. 1, the synchronverter with the appended damping correction loop consists of the active-power loop (Fig. 1(a)), the reactive-power loop (Fig. 1(b)), and the interface to the grid (Fig. 1(c)). We assume that the dc-bus voltage $u_{dc}$ remains constant due to the presence of sufficiently large energy storage devices (e.g., a battery or a supercapacitor) on the dc side. Below, we describe each subsystem in detail.

*1) Active-power loop:* The active-power loop (APL), as depicted in Fig. 1(a), emulates SG rotor dynamics modelled by the swing equation. Let $\omega_g$, $T_{ef}$, and $\psi_{ff}$, respectively, denote the rotating speed of the virtual rotor, the filtered electromagnetic torque, and the filtered excitation flux. The swing equation considering the damping correction loop is [6]

$$J_g \frac{d\omega_g}{dt} = T_m - T_{ef} - D_p(\omega_g - \omega_g^\star) - D_f \frac{d}{dt}\left(\frac{T_{ef}}{\psi_{ff}}\right), \quad (1)$$

where $J_g$ denotes the synthetic inertia constant, $T_m$ the input torque, and $\omega_g^\star$ the reference value of $\omega_g$. Suppose $P_t^\star$ denotes the reference value of the synchronverter active-power output $P_t$, and let $\omega_N$ represent the rated rotating speed. Then the input torque in (1) is $T_m = P_t^\star/\omega_N$. The term $-D_p(\omega_g - \omega_g^\star)$ in (1) models a simplified governor (neglecting the mechanical time-delay). If the frequency droop coefficient $D_p = 0$, $P_t$ tracks $P_t^\star$ with zero steady-state deviation; if $D_p > 0$, the APL achieves primary frequency control. Note that the value of $D_p$

is usually set by local grid codes based on the change in input torque required for a certain amount of frequency deviation, so $D_p$ may take different values depending on geographical location [2]. The term $D_f \frac{d}{dt}\left(\frac{T_{ef}}{\psi_{ff}}\right)$ represents the damping correction loop, which adjusts the synchronverter damping torque during the transient period. This can be deduced by neglecting the low-pass filters (LPFs), which are marked in red in Fig. 1(a), and noticing that $D_f \frac{d}{dt}\left(\frac{T_{ef}}{\psi_{ff}}\right)$ is proportional to $(\omega_g - \omega_\infty)$, where $\omega_\infty$ is the angular frequency of the grid voltage $u_\infty$ [6]. It is worth noting that the damping correction loop does not affect the steady-state frequency droop characteristics, as its steady-state value is zero. Finally, $T_{ef}$ and $\psi_{ff}$ are filtered signals that are obtained by

$$\tau_f \frac{dT_{ef}}{dt} = -T_{ef} + T_e, \tag{2}$$

$$\tau_f \frac{d\psi_{ff}}{dt} = -\psi_{ff} + \psi_f, \tag{3}$$

where $T_e = P_t/\omega_N$ is the electromagnetic torque, $\psi_f$ is the excitation flux, and $\tau_f$ is the time constant of the LPFs. The rotor angle is obtained as $\theta_g = \int_0^t \omega_g(\tau)d\tau$.

*2) Reactive-power loop:* As depicted in Fig. 1(b), the synchronverter reactive-power loop (RPL) governs the $\psi_f$ dynamics in order to regulate the reactive-power output $Q_t$ *or* the line-to-line RMS value $U_t$ of the terminal voltage $u_t$, depending on the states of Switches 1 and 2. The excitation flux $\psi_f$ dynamics are expressed as

$$K_g \frac{d\psi_f}{dt} = S_1(Q_t^\star - Q_{tf}) + S_2\sqrt{\frac{2}{3}}D_q(U_t^\star - U_{tf}), \tag{4}$$

where $K_g$ is a tuneable parameter, $Q_t^\star$ and $U_t^\star$ are, respectively, the reference values of $Q_t$ and $U_t$, $S_i$ $(i = 1, 2)$ represents the state of Switch $i$ ($S_i = 1$ corresponds to Switch $i$ being ON, and $S_i = 0$ to Switch $i$ being OFF). If the voltage droop coefficient $D_q = 0$ or $S_2 = 0$, then $Q_t$ tracks $Q_t^\star$ without steady-state error; if $D_q > 0$ and $S_2 = 1$, the RPL achieves voltage droop control. We assume that $D_q = 0$ in this paper, but this does not influence our analysis and results significantly. Finally, in (4), $Q_{tf}$ and $U_{tf}$ are, respectively, the filtered signals of $Q_t$ and $U_t$ and are expressed as

$$\tau_f \frac{dQ_{tf}}{dt} = -Q_{tf} + Q_t, \quad \tau_f \frac{dU_{tf}}{dt} = -U_{tf} + U_t. \tag{5}$$

*3) Grid interface:* As shown in Fig. 1(c), the synchronverter is interfaced to the external grid via a predominantly inductive filter with impedance $R_s + jX_s$ and a transmission line with impedance $R_e + jX_e$. We assume that the value of total reactance $X_t = X_s + X_e$ is much larger than that of the resistance $R_t = R_s + R_e$, which is valid for high-voltage transmission. With $\omega_g$, $\theta_g$, and $\psi_f$ obtained from the APL and RPL, the inner voltage $e_g$ is expressed as

$$e_g = \omega_g \psi_f \left[\sin\theta_g \quad \sin(\theta_g - \tfrac{2\pi}{3}) \quad \sin(\theta_g + \tfrac{2\pi}{3})\right]^{\mathrm{T}}, \tag{6}$$

and its line-to-line RMS value is $E_g = \sqrt{3/2}\omega_g\psi_f$. Let $\theta_{g\infty}$ denote the phase-angle difference between $e_g$ and $u_\infty$, and let $U_\infty$ denote the line-to-line RMS value of $u_\infty$. Then, $\theta_{g\infty}$ satisfies

$$\frac{d\theta_{g\infty}}{dt} = \omega_g - \omega_\infty, \tag{7}$$

and $T_e$, $Q_t$, and $U_t$ are, respectively, expressed as [6]

$$T_e = \frac{P_t}{\omega_N} \approx \sqrt{\frac{3}{2}}\frac{\psi_f U_\infty \sin\theta_{g\infty}}{X_t}, \tag{8}$$

$$Q_t = \frac{X_e}{X_t^2}E_g^2 - \frac{X_s}{X_t^2}U_\infty^2 + \frac{X_s - X_e}{X_t^2}E_g U_\infty \cos\theta_{g\infty}, \tag{9}$$

$$U_t = \sqrt{\frac{X_e^2}{X_t^2}E_g^2 + \frac{X_s^2}{X_t^2}U_\infty^2 + \frac{2X_eX_s}{X_t^2}E_g U_\infty \cos\theta_{g\infty}}. \tag{10}$$

### *B. Parameter Tuning with Small-signal Analysis [6]*

Based on the discussion in Section II-A, we note that the synchronverter APL dynamics are mainly influenced by parameters $J_g$, $D_p$, $D_f$, and $\tau_f$, which is evident from (1)–(3). Among these parameters, $D_p$ is set according to the local frequency regulation requirements, and $\tau_f$ is set to ensure that the LPFs have desired filtering abilities. In our previous work in [6], remaining parameters $J_g$ and $D_f$ are tuned by performing small-signal analysis on a model obtained from linearizing (1)–(5), and (7) around the equilibrium point $\boldsymbol{x}^\circ$, as follows: [6]

$$\frac{d\Delta\boldsymbol{x}}{dt} = \boldsymbol{A}\Delta\boldsymbol{x} + \boldsymbol{B}\Delta\boldsymbol{u}, \tag{11}$$

where the state vector $\Delta\boldsymbol{x}$ and input vector $\Delta\boldsymbol{u}$ are

$$\Delta\boldsymbol{x} = [\Delta\omega_g, \Delta\theta_{g\infty}, \Delta\psi_f, \Delta\psi_{ff}, \Delta T_{ef}, \Delta Q_{tf}, \Delta U_{tf}]^{\mathrm{T}},$$
$$\Delta\boldsymbol{u} = [\Delta P_t^\star, \Delta Q_t^\star, \Delta U_t^\star, \Delta\omega_g^\star, \Delta\omega_\infty]^{\mathrm{T}}, \tag{12}$$

respectively. In (12), $\Delta(\cdot)$ denotes small-signal perturbations in variable $(\cdot)$. Among the eigenvalues of $\boldsymbol{A}$, denoted by $\lambda_k$ $(k = 1, ..., 7)$, $\lambda_2 = -\alpha + j\beta$ and $\lambda_3 = -\alpha - j\beta$ represent the APL dominant mode, which is tuned by varying paramters $J_g$ and $D_f$ [6]. Via a numerical example below, we show that under two different operating conditions, $D_f$ influences the APL dominant mode in distinct ways.

**Example 1** (Impact of $D_f$ on the APL Dominant Mode)**.** In this example, for the system in Fig. 1, we adjust the APL dynamic response, which is mainly governed by the APL dominant mode, by varying parameter $D_f$ [6]. To highlight the impact of varying $D_f$ on the dominant mode under different operating conditions, we consider cases corresponding to two values of $D_p$, which may differ depending on different grid codes at different areas [3]. Values for other system parameters are adopted as reported in Appendix A. As shown in Fig. 2(a), if $D_p = 1407\ \mathrm{N\cdot m\cdot s/rad}$, increasing $D_f$ from $-4.0$ to $-2.5\ \mathrm{V\cdot s^2/rad}$ causes the damping ratio $\zeta$ of the APL dominant mode, represented by $\lambda_2$ and $\lambda_3$ of the full linearized system in (11), to increase from 0 to 1 [6]. On the other hand, the natural frequency $\omega_n$ of the APL dominant mode is minimally affected. This case is in accordance with expectations, since as derived in [6], omitting LPF and RPL dynamics yields a second-order APL model with damping ratio and natural frequency as follows: [19]

$$\zeta = \frac{\alpha}{\sqrt{\alpha^2+\beta^2}} \propto \frac{1}{\sqrt{J_g}}\left(D_p + D_f\sqrt{\frac{3}{2}}\frac{U_\infty \cos\theta_{g\infty}^{\mathrm{o}}}{X_t}\right),$$
$$\omega_n = \sqrt{\alpha^2+\beta^2} \propto \frac{1}{\sqrt{J_g}}, \tag{13}$$

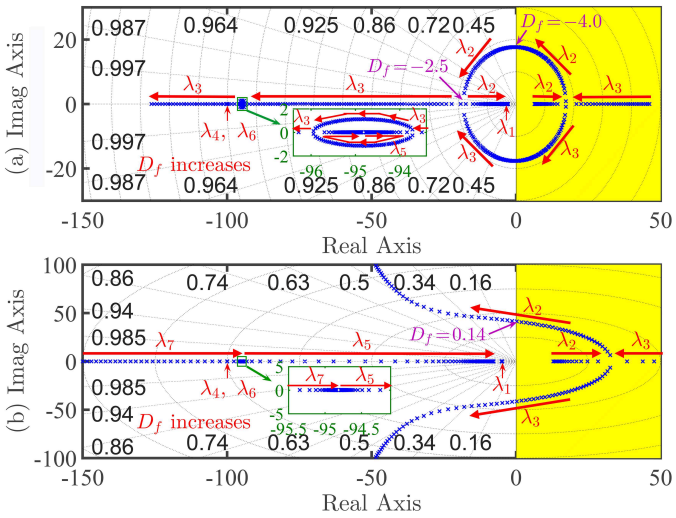


Fig. 2. Parameter $D_f$ influences APL dominant mode (represented by eigenvalues $\lambda_2$ and $\lambda_3$ of the full linearized system in (11)) differently depending on the operating condition. This results in more trial-and-error effort to tune synchronverter parameters via the iterative method in [6]. (a) With $D_p = 1407$, $D_f$ increases from $-6.5$ to 1. (b) With $D_p = 0$, $D_f$ increases from $-1.2$ to 2.

where the superscript $\circ$ denotes the equilibrium. Particularly, $D_f$ adjusts $\zeta$ freely without impacting $\omega_n$. In this way, the magnitude of $\lambda_2$ and $\lambda_3$ remains constant while their angles change, thus tracing out a circular path as $D_f$ varies, in accordance with the eigenvalue pattern observed in Fig. 2(a). On the other hand, if $D_p = 0$ N·m·s/rad, as shown in Fig. 2(b), $D_f$ does not tune $\zeta$ freely in the range $(0, 1)$, and it also influences $\omega_n$ significantly. This case is not captured by the relationships in (13). ■

### C. Problem Statement

As revealed in Example 1, varying the parameter $D_f$ influences the APL dominant mode differently under different operating conditions. Note that $J_g$ influences both $\zeta$ and $\omega_n$, as shown in (13) [6]. Thus, in the first case with $D_p = 1407$ N·m·s/rad, since $D_f$ mainly influences $\zeta$, we can tune $J_g$ and $D_f$ independently according to the desired $\omega_n$ and $\zeta$ via the iterative tuning process outlined in [6]. In the second case with $D_p = 0$, however, $\omega_n$ and $\zeta$ are both influenced by $D_f$ and cannot be adjusted independently using pararameters $J_g$ and $D_f$. In this case, (13) contradicts with the practical results, and further investigation is needed to explain the eigenvalue variation pattern in Fig. 2(b). Since the pattern in which $D_f$ affects eigenvalues is uncertain, the iterative tuning method in [6] leads to more trial-and-error work to achieve desired APL dominant-mode behaviour. In the next section, we develop a criterion to differentiate and predict the eigenvalue variation patterns due to changes in $D_f$ for different values of $D_p$. Subsequently, we propose to directly compute $J_g$ and $D_f$ based on desired $\omega_n$ and $\zeta$ characteristics.

## III. Proposed Parameter Tuning Method

This section presents two main contributions of this paper. First, we develop a criterion to explain and predict the impact of changes in parameter $D_f$ on eigenvalue variation patterns, specifically those of eigenvalues corresponding to the APL dominant mode. Then, we propose a method to directly compute $J_g$ and $D_f$ that satisfy prescribed damping ratio and natural frequency characteristics, which leads to desired APL time-domain response. This avoids the trial-and-error process and represents significant improvement over the iterative method in [6]. Here, instead of relying on the full linearized model in (11), we develop a third-order linearized model that captures pertinent system dynamic and steady-state behaviours. Such a reduced-order model is satisfactory when $X_t \gg R_t$, which leads to decoupled APL and RPL dynamics [3]. In this case, the roots of the characteristic equation of the third-order APL model accurately approximate the eigenvalues $\lambda_2$ and $\lambda_3$, which represent the APL dominant mode obtained from the original linearized model in (11).

Inspired by [20], here, we find that the key to ensuring the reduced-order model captures pertinent characteristics of the full-order model is to include LPF dynamics for the signal $T_e$ in addition to the rotor-angle dynamics. Since the APL transfer-function model in [6] neglects the LPF dynamics, it does not model the phenomenon uncovered in Example 1, and so cannot be used for accurate parameter tuning. With this in mind, we first get from (7) that

$$\omega_g = \frac{d\theta_{g\infty}}{dt} + \omega_\infty, \qquad \frac{d\omega_g}{dt} = \frac{d^2\theta_{g\infty}}{dt^2} + \frac{d\omega_\infty}{dt}. \tag{14}$$

Then, omitting the RPL dynamics in (4), setting $\psi_{ff} = \psi_f = \psi_f^\circ$, and assuming that $\omega_g^\star$ remains unchanged ($\Delta\omega_g^\star = 0$), we substitute (14) into (1) and linearize the resultant around the equilibrium point $\boldsymbol{x}^\circ$ to get the following small-signal model:

$$J_g\left(\frac{d^2\Delta\theta_{g\infty}}{dt^2} + \frac{d\Delta\omega_\infty}{dt}\right) = \frac{\Delta P_t^\star}{\omega_N} - \Delta T_{ef} - D_p\left(\frac{d\Delta\theta_{g\infty}}{dt} + \Delta\omega_\infty\right) - \frac{D_f}{\psi_f^\circ}\frac{d\Delta T_{ef}}{dt}. \tag{15}$$

Next, in order to account for the LPF dynamics for $T_e$, we substitute (8) into (2), and then linearize (2) around $\boldsymbol{x}^\circ$ to get

$$\tau_f\frac{d\Delta T_{ef}}{dt} = -\Delta T_{ef} + \sqrt{\frac{3}{2}}\frac{\psi_f^\circ U_\infty\cos\theta_{g\infty}^\circ}{X_t}\Delta\theta_{g\infty}. \tag{16}$$

By taking the Laplace transformation of (15) and (16), and solving them for $\Delta\theta_{g\infty}$, we get the following input-output relationship for the reduced third-order APL model:

$$\Delta\theta_{g\infty} = \frac{(\tau_f s + 1)\left(\Delta P_t^\star - \omega_N(J_g s + D_p)\Delta\omega_\infty\right)}{\tau_f J_g\omega_N\cdot(s^3 + bs^2 + Ks + d)}, \tag{17}$$

where

$$b = \frac{J_g + \tau_f D_p}{\tau_f J_g}, \tag{18}$$

$$K = \frac{1}{\tau_f J_g}\left(D_p + D_f\sqrt{\frac{3}{2}}\frac{U_\infty\cos\theta_{g\infty}^\circ}{X_t}\right), \tag{19}$$

$$d = \sqrt{\frac{3}{2}}\frac{\psi_f^\circ U_\infty\cos\theta_{g\infty}^\circ}{\tau_f J_g X_t}. \tag{20}$$

The characteristic equation of the model in (17) is

$$s^3 + bs^2 + Ks + d = 0. \tag{21}$$

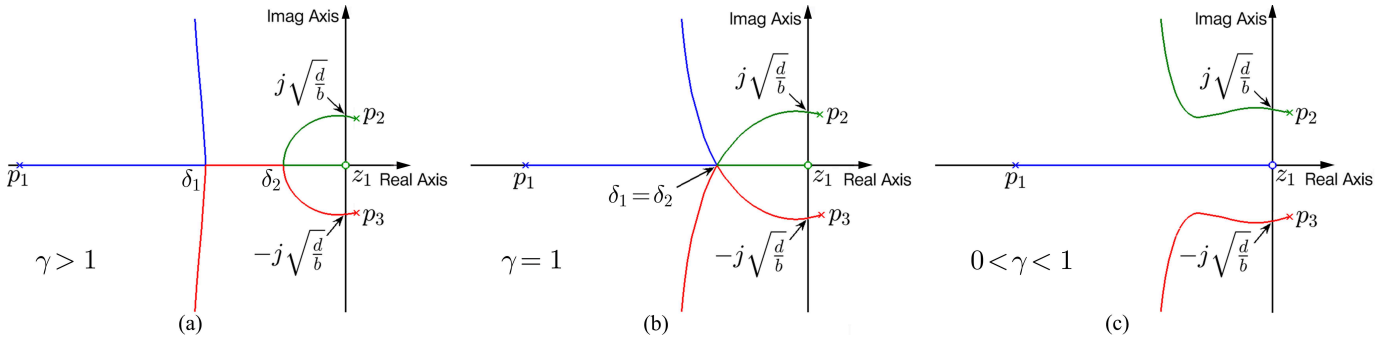


Fig. 3. Different root loci patterns of $1 + KG(s) = 0$ in the $s$-plane with (a) $\gamma > 1$, (b) $\gamma = 1$, and (c) $0 < \gamma < 1$.

Note that if the LPF dynamics were neglected as in [6], we would obtain a second-order model with lower accuracy. Next, we conduct root locus analysis for (21), which helps to establish a criterion to predict the pattern in which $D_f$ affects the roots of (21), and in turn, the APL dominant mode of the full model in (11).

### A. Criterion for Different Eigenvalue Variation Patterns

By performing root locus analysis on the characteristic equation in (21), we evaluate the influence of varying $D_f$ on the APL dominant mode under different operating conditions. The eigenvalue variation patterns resulting from varying $D_f$ can be categorized into three different types, depending on the number of breakaway points (0, 1, or 2) in the root loci.

The root locus analysis begins by rewriting (21) as

$$1 + KG(s) = 0, \tag{22}$$

where

$$G(s) = \frac{s}{s^3 + bs^2 + d}. \tag{23}$$

According to (19), $K$ is a linear function of $D_f$, so variations in $D_f$ and $K$ produce the same trends on the root loci of (22). Moreover, according to (21), $K > 0$ is a necessary condition for the system in (17) to be stable. Thus, we increase $K$ from 0 to $+\infty$ (by varying $D_f$), and determine the root loci [21]. Please refer to Appendix B for details of the root locus analysis, which is summarized as Fig. 3.

Based on the analysis in Appendix B, we find that as $D_f$ varies, the root loci of $1 + KG(s) = 0$ have three different types of patterns depending on the value of

$$\gamma := \frac{1}{3}\sqrt[3]{\sqrt{\frac{2}{3}}\frac{X_t}{\psi_f^\circ U_\infty \cos\theta_{g\infty}^\circ}}\left(\sqrt[3]{\frac{J_g}{\tau_f^2}} + D_p\sqrt[3]{\frac{\tau_f}{J_g^2}}\right). \tag{24}$$

These cases are summarized as follows: (i) if $\gamma > 1$, as shown in Fig. 3(a), the root loci of (22) have two breakaway points $\delta_1$ and $\delta_2$, (ii) if $\gamma = 1$, as shown in Fig. 3(b), the root loci of (22) have one breakaway point $\delta_1 = \delta_2$, and (iii) if $0 < \gamma < 1$, as shown in Fig. 3(c), the root loci of (22) have no breakaway points. Note that only if $\gamma \geq 1$ can the damping ratio of the APL dominant mode be tuned freely in the range $(0, 1)$ by varying only $D_f$. In the remainder of the paper, we refer to these conclusions on $\gamma$ as the $\gamma$-criterion. As $D_f$ varies, the two branches of the root loci beginning at $p_2$ and $p_3$ correspond to the trajectories of $\lambda_2$ and $\lambda_3$ in the eigenvalue variation patterns, which can be verified using (11). Thus, we can readily use the $\gamma$-criterion developed from the third-order model to predict the eigenvalue variation patterns of $\lambda_2$ and $\lambda_3$ due to changes in $D_f$.

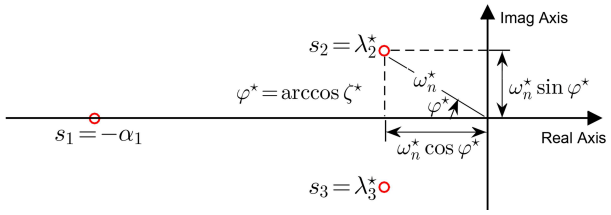


Fig. 4. Desired APL pole locations in the $s$-plane used to directly compute parameters $J_g$ and $D_f$.

**Example 2** (Differentiating Eigenvalue Variation Patterns)**.** The proposed $\gamma$-criterion can be used to explain the different eigenvalue variation patterns resulting from varying $D_f$ in Example 1. In the first case where $D_p = 1047\ \mathrm{N \cdot m \cdot s/rad}$, we have that $\gamma = 3.58 > 1$ (i.e., Fig. 3(a)). Indeed, as shown in Fig. 2(a), varying only $D_f$ adjusts the damping ratio of the APL dominant mode freely in the range $(0, 1)$. On the other hand, in the case where $D_p = 0$, we have that $\gamma = 0.60 \in (0, 1)$ (i.e., Fig. 3(c)). Accordingly, as shown in Fig. 2(b), tuning only $D_f$ cannot adjust the damping ratio of the APL dominant mode freely in the range $(0, 1)$. Moreover, as predicted in Fig. 3(c), the root loci go to $\infty$ along the asymptotes as $K$ (or $D_f$) increases. Thus, in this case, variations in $D_f$ also significantly influence $\omega_n$. ■

With the proposed $\gamma$-criterion in place, we are able to predict the effects of $D_f$ variations on eigenvalues of (11) corresponding to the APL dominant mode under different operating conditions. Next, in order to avoid the shortcoming of the iterative tuning method in [6], we propose a method to compute APL parameters $J_g$ and $D_f$ directly to satisfy prescribed damping ratio and natural frequency requirements.

### B. Direct Computation of APL Parameters

Here, we propose a direct computation method to obtain the APL parameters $J_g$ and $D_f$ for given APL dominant mode requirements, regardless of the value of $\gamma$. Using this method, we avoid the trial-and-error process in tuning the

APL parameters, which plagued the iterative method in [6]. First, denote $\zeta^\star$ and $\omega_n^\star$ as, respectively, the required damping ratio and natural frequency for the APL dominant mode. Also denote $\varphi^\star = \arccos\zeta^\star \in (0, \pi/2)$. Then, as depicted in Fig. 4, the desired APL dominant pole locations are

$$\begin{aligned}\lambda_2^\star &= -\omega_n^\star\cos\varphi^\star + j\omega_n^\star\sin\varphi^\star,\\ \lambda_3^\star &= -\omega_n^\star\cos\varphi^\star - j\omega_n^\star\sin\varphi^\star.\end{aligned} \tag{25}$$

The proposed direct computation method leverages the fact that the poles of the third-order system in (17) closely approximate the APL dominant mode, which is represented by $\lambda_2$ and $\lambda_3$ (eigenvalues of the full linearized system in (11)). In this way, we translate the problem of achieving desired pole locations for the full system in (11) to one for the reduced third-order system in (17). To this end, denote poles of (17) (or the roots of (21)) as $s_1$, $s_2$, and $s_3$. By tuning $J_g$ and $D_f$, we wish to place two complex-conjugate roots of the characteristic equation in (21) at the locations of $\lambda_2^\star$ and $\lambda_3^\star$ in the $s$-plane, so we set $s_2 = \lambda_2^\star$ and $s_3 = \lambda_3^\star$. Further set $s_1 = -\alpha_1$ ($\alpha_1 > 0$), which is an unspecified real-valued root of (21). Then, according to Vieta's formulas [22], for (21), we have

$$-b = s_1 + s_2 + s_3 = -\alpha_1 - 2\omega_n^\star\cos\varphi^\star, \tag{26}$$

$$K = s_1s_2 + s_2s_3 + s_1s_3 = 2\alpha_1\omega_n^\star\cos\varphi^\star + {\omega_n^\star}^2, \tag{27}$$

$$-d = s_1s_2s_3 = -\alpha_1{\omega_n^\star}^2, \tag{28}$$

where the second equality in each of (26)–(28) results by substituting $s_2 = \lambda_2^\star$ and $s_3 = \lambda_3^\star$ from (25), as well as $s_1 = -\alpha_1$. Recall that $b$, $K$, and $d$ are functions of $J_g$ and $D_f$ according to (18), (19), and (20), so $\alpha_1$, $J_g$, and $D_f$ are the three unknown variables in (26)–(28) for which to be solved. We first obtain from (28) that

$$\alpha_1 = d/{\omega_n^\star}^2. \tag{29}$$

Then, by substituting (29) into (26) and (27), and then solving them for $J_g$ and $D_f$, we get the following *closed-form* expressions for tuneable controller parameters $J_g$ and $D_f$:

$$J_g = \frac{\sqrt{\frac{3}{2}}\psi_f^\circ U_\infty\cos\theta_{g\infty}^\circ - \tau_f D_p X_t {\omega_n^\star}^2}{{\omega_n^\star}^2 X_t(1-2\tau_f\omega_n^\star\zeta^\star)}, \tag{30}$$

$$\begin{aligned}D_f =& \frac{2\psi_f^\circ\zeta^\star}{\omega_n^\star} + \frac{\tau_f\psi_f^\circ}{1-2\tau_f\omega_n^\star\zeta^\star}\\ &- \sqrt{\frac{2}{3}}\frac{X_tD_p}{U_\infty\cos\theta_{g\infty}^\circ}\left(1 + \frac{{\tau_f}^2{\omega_n^\star}^2}{1-2\tau_f\omega_n^\star\zeta^\star}\right),\end{aligned} \tag{31}$$

which achieve the desired pole locations as defined in (25). Note that $J_g$ and $D_f$ can be recomputed easily for different operating points. In fact, through extensive simulations, we find that these parameters do not vary significantly over the range of normal operating points.

After obtaining the APL parameters $J_g$ and $D_f$ with (30) and (31), we verify that $J_g > 0$ and $s_1 < \mathrm{Re}(s_2)$. Among these two requirements, $J_g$ must be positive since $J_g \le 0$ causes the system to be unstable. The condition $s_1 < \mathrm{Re}(s_2)$ ensures that $s_2$ and $s_3$ represent the APL dominant mode as shown in Fig. 4. If $J_g \le 0$ or $s_1 \ge \mathrm{Re}(s_2)$, the prescribed $\omega_n^\star$ is too large and must be reduced. The conditions on $\omega_n^\star$ are not within the scope of this paper, but we reserve this as an important avenue of future work.

**Remark 1** (Effective Inertia and Damping Constants)**.** Due to the effects of the damping correction loop in the modified APL swing equation in (1) and the LPF dynamics, $J_g$ alone does not fully capture the synchronverter inertia characteristic. In this remark, we characterize the *effective* synchronverter inertia and damping. With $J_g$ and $D_f$ chosen as in (30) and (31), respectively, and assuming that $\Delta\omega_\infty = 0$, (17) can be expressed as

$$\begin{aligned}\Delta\theta_{g\infty} =& \frac{(\tau_f s+1)\,\Delta P_t^\star}{\tau_f J_g\omega_N\cdot(s-s_1)(s-s_2)(s-s_3)}\\ =& \frac{(\tau_f s+1)\,\Delta P_t^\star}{\tau_f J_g\omega_N\alpha_1(\frac{1}{\alpha_1}s+1)\left(s^2+2\zeta^\star\omega_n^\star s+{\omega_n^\star}^2\right)}.\end{aligned} \tag{32}$$

In practice, $\alpha_1 \gg 1$, and moreover, the dynamics associated with the pole $s_1 = -\alpha_1$ are faster than those associated with poles $s_2$ and $s_3$, so here, we approximate $\frac{1}{\alpha_1}s+1 \approx 1$ in (32) [21]. Also, it turns out that by choosing $\tau_f$ to satisfy noise rejection requirements, $0 < \tau_f \ll 1$ and the zero $-1/\tau_f$ is sufficiently far away from the APL dominant poles, so its effect on the time-domain response is small, and we approximate $\tau_f s+1 \approx 1$ in (32) [21]. With these assumptions in place, inverse Laplace transformation of (32) yields

$$\frac{d^2\Delta\theta_{g\infty}}{dt^2} = \frac{\Delta P_t^\star}{\tau_f J_g\omega_N\alpha_1} - 2\zeta^\star\omega_n^\star\frac{d\Delta\theta_{g\infty}}{dt} - {\omega_n^\star}^2\Delta\theta_{g\infty}. \tag{33}$$

Next, to incorporate $\Delta T_e$ into (33), linearize (8) with respect to $\theta_{g\infty}$ to get

$$\Delta T_e = \sqrt{\frac{3}{2}}\frac{\psi_f^\circ U_\infty\cos\theta_{g\infty}^\circ}{X_t}\Delta\theta_{g\infty}. \tag{34}$$

Also, since $\Delta\omega_\infty = 0$, we have from (14) that

$$\Delta\omega_g = \frac{d\Delta\theta_{g\infty}}{dt}, \qquad \frac{d\Delta\omega_g}{dt} = \frac{d^2\Delta\theta_{g\infty}}{dt^2}. \tag{35}$$

Solving for $\Delta\theta_{g\infty}$ in (34) and substituting the resultant along with (35) and (29) into (33), we get that

$$J_{\mathit{eff}}\frac{d\Delta\omega_g}{dt} = \Delta T_m - \Delta T_e - D_{\mathit{eff}}\Delta\omega_g, \tag{36}$$

where $\Delta T_m = \Delta P_t^\star/\omega_N$, the *effective inertia constant* is

$$J_{\mathit{eff}} = \sqrt{\frac{3}{2}}\frac{\psi_f^\circ U_\infty\cos\theta_{g\infty}^\circ}{X_t}\cdot\left(\frac{1}{\omega_n^\star}\right)^2, \tag{37}$$

and the *effective damping constant* is

$$D_{\mathit{eff}} = \sqrt{6}\psi_f^\circ U_\infty\cos\theta_{g\infty}^\circ\cdot\left(\frac{\zeta^\star}{\omega_n^\star}\right). \tag{38}$$

Note that, according to (37), $J_{\mathit{eff}} \propto (1/\omega_n^\star)^2$ and $J_{\mathit{eff}}$ is independent of the desired APL damping ratio $\zeta^\star$. Thus, in our proposed method, by specifying the natural frequency $\omega_n^\star$ for the APL dominant poles, we conveniently achieve the desired inertia characteristic. We also note that the effective inertia $J_{\mathit{eff}}$ may be larger, smaller, or the same as the inertia constant $J_g$, depending on the system parameters, operating point, and desired time-domain performance. Once the desired $J_{\mathit{eff}}$ is satisfied, the desired effective damping constant $D_{\mathit{eff}}$ can be achieved by specifying $\zeta^\star$, in accordance with (38). ■

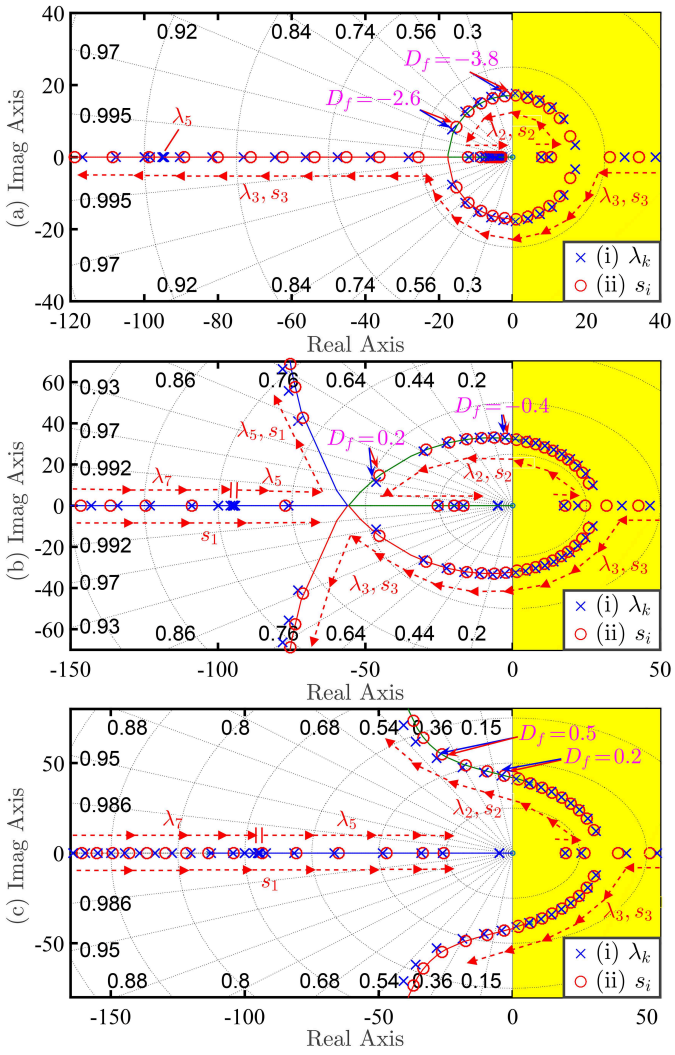


Fig. 5. Verification of the reduced third-order APL model and the proposed $\gamma$-criterion in the $s$-plane, i.e., varying $D_f$ influences the APL damping ratio differently when $\gamma$ takes values in different ranges. Particularly, only when $\gamma \geq 1$ can the APL damping ratio be adjusted freely in the range $(0, 1)$. (a) $\gamma = 3.58$, $-6.2 \leq D_f \leq 0.7$ ($J_g = 2.814$, $D_p = 1407.0$, $\tau_f = 0.01$). (b) $\gamma = 1.00$, $-1.6 \leq D_f \leq 0.5$ ($J_g = 2.814$, $D_p = 190.25$, $\tau_f = 0.01$). (c) $\gamma = 0.60$, $-0.9 \leq D_f \leq 0.7$ ($J_g = 2.814$, $D_p = 0$, $\tau_f = 0.01$).

### C. Summary of Proposed Parameter Tuning Method

Based on the discussion above, we propose to tune the synchronverter APL parameters $D_p$, $\tau_f$, $J_g$, and $D_f$ as follows. First, $D_p$ is specified to satisfy local grid frequency-droop requirements, which may differ in different geographical locations. Next, we choose $\tau_f$ based on the LPF noise rejection requirements. Then, according to the desired $\omega_n^\star$ and $\zeta^\star$ of the APL dominant mode, we compute $J_g$ and $D_f$ using (30) and (31). Finally, with the chosen parameter values, we verify that (i) $J_g > 0$ and (ii) $s_1 < \mathrm{Re}(s_2)$. Note that the RPL parameters can still be chosen based on the method proposed in [2]. In the next section, we validate the proposed $\gamma$-criterion and the direct computation method.

## IV. Case Studies

In this section, we first verify that two complex-valued roots of the characteristic equation for the third-order model closely approximate eigenvalues $\lambda_2$ and $\lambda_3$ of the full linearized model in (11), which represent the APL dominant mode. We also show that the proposed $\gamma$-criterion accurately predicts the eigenvalue variation patterns resulting from varying $D_f$. Then, via several case studies, we verify that the proposed direct computation method is highly effective in obtaining the APL parameters and placing the eigenvalues $\lambda_2$ and $\lambda_3$ at their respective desired locations. Moreover, we validate that in actual grid conditions, the proposed direct computation method is still effective in achieving desired APL response speed. The system under study in Sections IV-A and IV-B is the single-synchronverter infinite-bus system shown in Fig. 1, with parameter values reported in Appendix A, unless otherwise specified. The system under study in Section IV-C is a six-bus test system, with component parameters provided in Appendix C.

TABLE I
Direct Computation of APL Parameters $J_g$ and $D_f$

| | Desired $\lambda_2^\star$ and $\lambda_3^\star$ | $J_g$ | $D_f$ | Actual $\lambda_2$ and $\lambda_3$ | Error $\epsilon$ |
|---|---|---|---|---|---|
| 1 | $-9.239 \pm j3.827$ | 57.86 | 2.221 | $-9.380 \pm j4.076$ | 2.86% |
| 2 | $-7.071 \pm j7.071$ | 54.94 | 1.602 | $-7.194 \pm j7.057$ | 1.24% |
| 3 | $-3.827 \pm j9.239$ | 51.08 | 0.6781 | $-3.952 \pm j9.188$ | 1.36% |
| 4 | $-18.48 \pm j7.654$ | 16.44 | 0.9433 | $-18.31 \pm j7.801$ | 1.11% |
| 5 | $-14.14 \pm j14.14$ | 14.45 | 0.6154 | $-14.27 \pm j13.99$ | 0.982% |
| 6 | $-7.654 \pm j18.48$ | 12.24 | 0.1334 | $-7.929 \pm j18.41$ | 1.42% |
| 7 | $-27.72 \pm j11.48$ | 7.965 | 0.5269 | $-27.34 \pm j11.24$ | 1.49% |
| 8 | $-21.21 \pm j21.21$ | 6.166 | 0.2770 | $-21.57 \pm j20.82$ | 1.78% |
| 9 | $-11.48 \pm j27.72$ | 4.608 | $-0.06764$ | $-12.08 \pm j27.71$ | 1.98% |

### A. Verifying the Reduced-order Model and the $\gamma$-Criterion

In this case study, we vary $D_f$ with $D_p$ taking values of 1407.0, 190.25, and 0 $\mathrm{N \cdot m \cdot s/rad}$, and correspondingly, Figs. 5(a)–(c) show the trajectories of the APL characteristic equation roots $s_i$ ($i = 1, 2, 3$) and the state matrix $\boldsymbol{A}$ eigenvalues $\lambda_k$ ($k = 1, ..., 7$). In Fig. 5, $s_i$ and $\lambda_k$ are, respectively, marked with $\circ$ and $\times$, and the root loci of $1 + KG(s) = 0$ are indicated by the solid lines. Note that $\gamma > 1$ when $D_p > 190.25$ $\mathrm{N \cdot m \cdot s/rad}$, $\gamma = 1$ when $D_p = 190.25$ $\mathrm{N \cdot m \cdot s/rad}$, and $\gamma < 1$ when $D_p < 190.25$ $\mathrm{N \cdot m \cdot s/rad}$.

Based on visual inspection of Fig. 5, we make two observations. First, the roots $s_2$ and $s_3$ of (21) and the eigenvalues $\lambda_2$ and $\lambda_3$ of the state matrix $\boldsymbol{A}$ in (11) are well matched. Thus, the reduced third-order APL model in (17) is sufficiently accurate, and its characteristic equation roots $s_2$ and $s_3$ provide satisfactory approximations for $\lambda_2$ and $\lambda_3$, which represent the APL dominant mode. Moreover, with $\gamma \geq 1$ (as shown in Figs. 5(a)(b)), the trajectories of $s_2$ and $s_3$ (and those of $\lambda_2$ and $\lambda_3$) have at least one breakaway point in the left half $s$-plane. Otherwise, when $0 < \gamma < 1$ (as shown in Fig. 5(c)), the trajectories of $s_2$ and $s_3$ (and also $\lambda_2$ and $\lambda_3$) have no breakaway points in the left half-plane. In other words, varying $D_f$ adjusts the damping ratio of the APL dominant mode freely in the range $(0, 1)$ only when $\gamma \geq 1$. This agrees well with the root locus analysis results summarized in Fig. 3. Thus, we conclude that the proposed $\gamma$-criterion

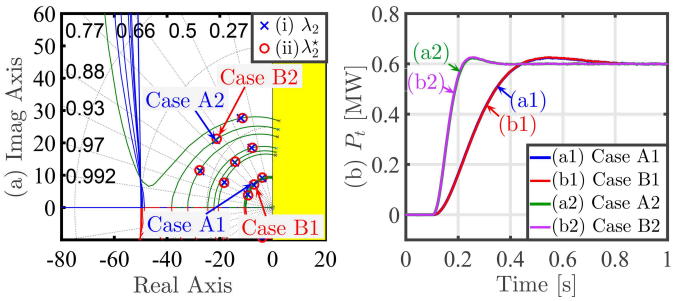


Fig. 6. Verification of the proposed direct computation method achieving (a) accurate APL pole placement in the $s$-plane. (b) desired APL dynamic response in the time domain.

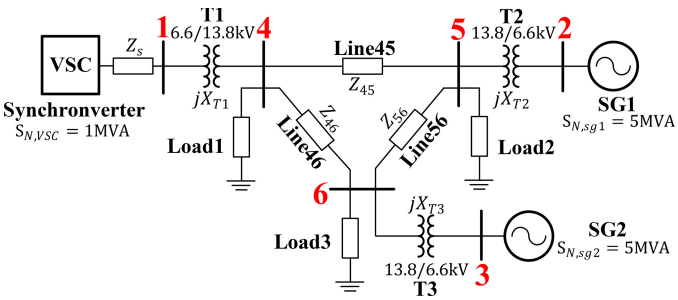


Fig. 7. Six-bus test system used to verify the proposed parameter computation method.

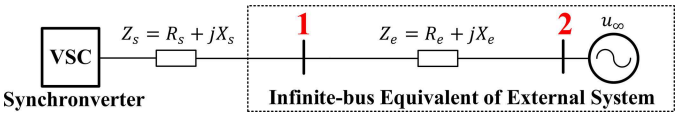


Fig. 8. Equivalent single-synchronverter infinite-bus system obtained from six-bus test system via network reduction.

indeed accurately predicts the eigenvalue variation patterns arising from varying $D_f$.

### *B. Validating the Proposed Parameter Computation Method*

In this case study, via comparison with the iterative tuning method in [6], we demonstrate the accuracy and effectiveness of the proposed direct computation method. The comparisons are summarized in Table I, in which (i) the natural frequency $\omega_n^\star$ of the desired APL dominant mode in rows 1–3, rows 4–6, and rows 7–9 are, respectively, 10, 20, and 30; and (ii) the damping ratio $\zeta^\star$ of the desired APL dominant mode in rows $(3m+1)$, rows $(3m+2)$, and rows $(3m+3)$ are, respectively, 0.924, 0.707, and 0.383 ($m = 0, 1, 2$). Based on these desired characteristics, we compute the APL parameters $J_g$ and $D_f$ using (30) and (31). Next, we substitute the resulting $J_g$ and $D_f$ into the state matrix $\boldsymbol{A}$, and compute the eigenvalues $\lambda_2$ and $\lambda_3$. We also obtain the relative error $\epsilon$ between the desired $\lambda_2^\star$ and the actual $\lambda_2$ according to

$$\epsilon = \frac{\|\lambda_2^\star - \lambda_2\|}{\|\lambda_2^\star\|} \times 100\%. \tag{39}$$

The resulting $J_g$, $D_f$, $\lambda_2$, $\lambda_3$, and $\epsilon$ for all cases are reported in Table I, and both the desired $\lambda_2^\star$ and the actual $\lambda_2$ are plotted in Fig. 6(a) for comparison. By graphically comparing $\lambda_2^\star$ and $\lambda_2$, we find that they are well matched. Moreover, their relative errors $\epsilon$ are all less than 3%. This is also true for $\lambda_3^\star$ and $\lambda_3$. Thus, we conclude that, with the proposed method, we can directly compute $J_g$ and $D_f$ to effectively place the eigenvalues $\lambda_2$ and $\lambda_3$, which represent the APL dominant mode, at their desired locations $\lambda_2^\star$ and $\lambda_3^\star$ with minimal error.

Via time-domain simulations, we show that the minor errors between actual and desired eigenvalues do not cause noticeable differences in the APL dynamic response. We take cases corresponding to rows 2 and 8 in Table I as examples. Using the iterative tuning method in [6], we find that when $J_g = 55.66\ \text{kg}\cdot\text{m}^2$ and $D_f = 1.597\ \text{V}\cdot\text{s}^2/\text{rad}$, $\lambda_2$ and $\lambda_3$ are exactly equal to desired $\lambda_2^\star$ and $\lambda_3^\star$ in row 2 (Case B1). Via a similar method, when $J_g = 6.081\ \text{kg}\cdot\text{m}^2$ and $D_f = 0.2627\ \text{V}\cdot\text{s}^2/\text{rad}$, $\lambda_2$ and $\lambda_3$ are exactly equal to desired $\lambda_2^\star$ and $\lambda_3^\star$ in row 8 (Case B2). We model the synchronverter-connected system as shown in Fig. 1 in the PSCAD/EMTDC. At $t = 0.1$ s, the active-power reference value $P_t^\star$ increases from 0 MW to 0.6 MW. Figure 6(b) shows the time-domain simulation results when we adopt 4 different set of parameters $J_g$ and $D_f$. Cases A1 and A2 use the APL parameters computed from (30) and (31) in rows 2 and 8, respectively, of Table I. Cases B1 and B2 adopt the APL parameters obtained with the iterative tuning method. As shown in Fig. 6(b), traces (a1) and (b1), which correspond to Cases A1 and B1, respectively, are nearly identical. This is also true for traces (a2) and (b2), which correspond to Cases A2 and B2. Thus, we conclude that the APL parameters obtained from the proposed direct computation method achieve desired APL dynamic response.

### *C. Applying the Proposed Parameter Computation Method*

To further validate the proposed method, we implement it to tune parameters of a synchronverter connected to a six-bus system with one-line diagram shown in Fig. 7. In this system. a synchronverter and two SGs (SG1 and SG2) supply power, via three transformers (T1, T2, and T3, respectively), to three constant-impedance loads (Load1, Load2, and Load3) in the system. Generators SG1 and SG2 are each equipped with a Woodward governor (see Fig. 10) to achieve primary frequency control and a standard excitation system (see Fig. 11) to regulate terminal voltages. The high-voltage sides of transformers T1, T2, and T3 are, respectively, connected to buses 4–6. Three transmission lines (Line45, Line46, and Line56) connect buses 4–6, forming a ring structure.

Since the proposed direct computation method is based on a single-synchronverter infinte-bus system as shown in Fig. 1(c), here, we compute an infinite-bus equivalent of the external system as seen from the synchronverter via network reduction. First, we use Kron reduction [23] to eliminate buses 4–6 in the test system, since they are connected to only passive components. Then, following the method proposed in [24], we further merge buses 2 and 3, and get an equivalent single-synchronverter infinite-bus system shown in Fig. 8, in which the infinite-bus voltage is $U_\infty = 6.80$ kV, and the equivalent impedance is $Z_e \approx jX_e = j3.45\ \Omega$ (we retain only the

TABLE II
CASES I–IV USED TO VERIFY THE PROPOSED DIRECTION COMPUTATION METHOD IN ACTUAL GRID CONDITIONS

| Case | Desired APL response speed | $\omega_n^\star$ (rad/s) | $\zeta^\star$ | $H_{sg1}$ (s) | $H_{sg2}$ (s) | System inertia level |
|---|---|---|---|---|---|---|
| I | fast | 30.0 | 0.707 | 8.00 | 8.00 | high |
| II | fast | 30.0 | 0.707 | 3.00 | 3.00 | low |
| III | slow | 10.0 | 0.707 | 8.00 | 8.00 | high |
| IV | slow | 10.0 | 0.707 | 3.00 | 3.00 | low |

reactance $X_e$, since the network in Fig. 7 is assumed to be predominantly inductive).

Using the infinite-bus equivalent of the external system, we tune the APL parameters $J_g$ and $D_f$ with the proposed method in four different cases, as summarized in Table II ($H_{sg1}$ and $H_{sg2}$, respectively, denote the SG1 and SG2 inertia time constant). In cases I and II, the synchronverter is tuned to respond quickly with $\omega_n^\star = 30.0$ rad/s and $\zeta^\star = 0.707$, and in cases III and IV, the synchronverter is tuned to respond slowly with $\omega_n^\star = 10.0$ rad/s and $\zeta^\star = 0.707$. The system has high inertia in cases I and III and low inertia in cases II and IV. In all four cases, we set $D_p = 0$ N · m · s/rad so that the actual and desired APL dynamic responses can be compared conveniently. Then, using (30) and (31), we directly compute APL parameters $J_g = 21.4$ kg · m$^2$ and $D_f = 0.953$ V · s/rad in cases I and II, and $J_g = 129$ kg · m$^2$ and $D_f = 2.26$ V · s/rad in cases III and IV. Note that the computed APL parameters are the same in cases I and II (or cases III and IV), since our method does not depend on system inertia.

With synchronverter parameters for cases I–IV summarized in Appendix C, we simulate the six-bus test system in Fig. 7 in PSCAD/EMTDC. In each case, the synchronverter active-power reference value $P_t^\star$ increases from 0.0 MW to 0.6 MW at $t = 1.0$ s. The resulting APL output $P_t$ in cases I–IV are marked as trace (i) in Figs. 9(a)–(d), respectively. In order to validate the proposed method in actual grid conditions, we also plot the corresponding desired $P_t$ response as trace (ii) in Fig. 9. Note that we obtain the desired $P_t$ response in each case from the single-synchronverter infinite-bus system using APL parameters tuned via the iterative tuning method in [6] to achieve the desired $\omega_n^\star$ and $\zeta^\star$ precisely.

As shown in Figs. 9(a) (case I) and (b) (case II), when the synchronverter is tuned to respond quickly, in both high- and low-inertia systems, there is little discrepancy between the actual $P_t$ (trace (i) in Figs. 9(a) and (b)) and the corresponding desired response (trace (ii) in Figs. 9(a) and (b)). This verifies our proposed method to accurately tune the synchronverter parameters to achieve desired fast time-domain response in cases with high and low levels of system inertia.

As shown in Figs. 9(c) (case III) and (d) (case IV), when the synchronverter is tuned to respond slowly, there are larger deviations between the actual $P_t$ (trace (i) in Figs. 9(c) and (d)) and its desired response (trace (ii) in Figs. 9(c) and (d)). In these cases, when the synchronverter is tuned to respond slowly, its APL dynamics act in similar time scales as those of SG1 and SG2 rotors. We also note that the deviations in case IV are larger than those in case III, because the lower inertia level in case IV brings the SG rotor dynamics even closer in time scales with the APL dynamics. In contrast, the fast APL dynamics in cases I and II are essentially decoupled from the comparatively slower SG rotor dynamics. Even though there are larger deviations in cases III and IV, we highlight that the desired response speed is achieved immediately following the increase in $P_t^\star$ at $t = 1.0$ s. Thus, we verify the efficacy of the proposed direct computation method where slower response speed is desirable.

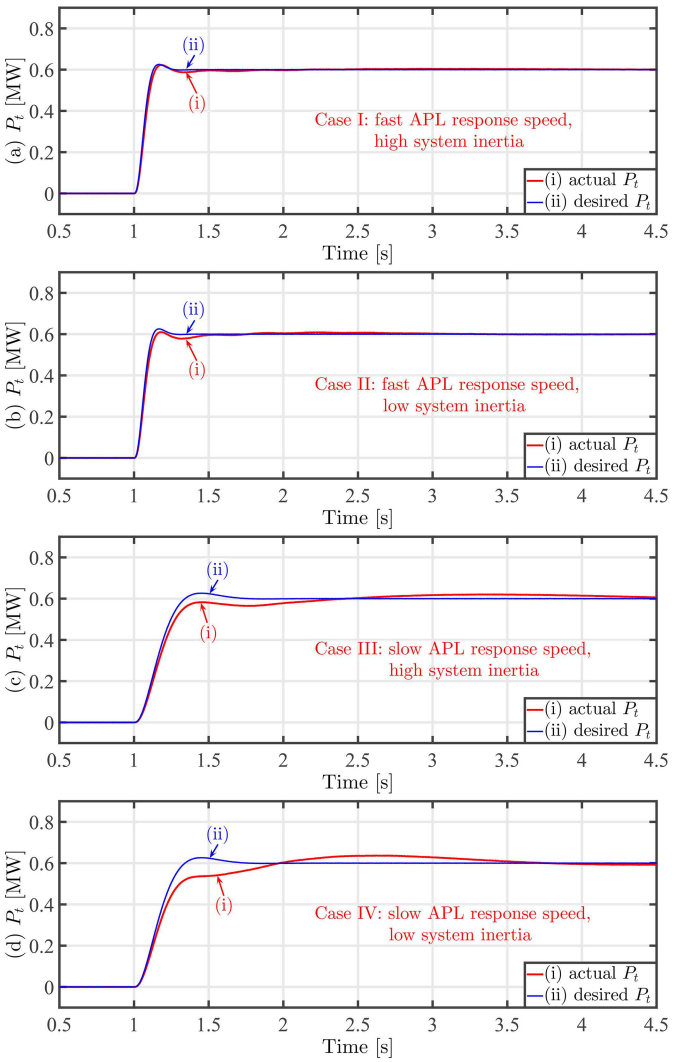


Fig. 9. Verification of the proposed direct computation method to achieve desired APL dynamic responses in actual grid conditions by comparing the time-domain responses between the actual and desired $P_t$ in cases (a) I, (b) II, (c) III, and (d) IV.

## V. CONCLUDING REMARKS

This paper identifies a shortcoming in tuning the synchronverter APL parameters with the iterative method based on small-signal analysis. Specifically, varying $D_f$ influences the APL dominant mode differently under different operating conditions, and so more trial-and-error work is needed during the parameter tuning process. In order to explain this phenomenon, we develop a precise criterion to differentiate between possible eigenvalue variation patterns. Moreover, we

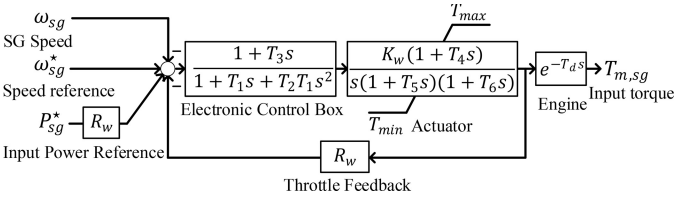


Fig. 10. Modified Woodward governor used in SG1 and SG2 to achieve primary frequency regulation [25].

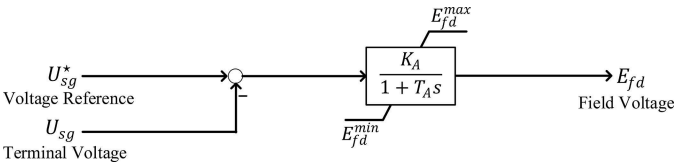


Fig. 11. Excitation system used in SG1 and SG2 to control their terminal voltages [26].

propose a method to directly compute the APL parameters $J_g$ and $D_f$, and in turn achieve desired APL dominant-mode behaviour. Unlike previous VSG parameter tuning methods, the proposed method directly computes parameter values that achieve desired transient and steady-state behaviour, and in so doing, greatly simplifies the tuning process. Nevertheless, the proposed method has two limitations: (i) it does not capture how the synchronverter interacts with actual SGs in the desired APL time-domain response, and (ii) it assumes that external grid is predominantly inductive, which may not hold for low-voltage distribution systems. Directions for future work include (i) determining feasible locations of APL dominant poles in the $s$-plane, (ii) applying the proposed method to tune other VSG designs, and (iii) combining with parameter estimation methods to achieve adaptive control.

## APPENDIX

### A. Parameters of Synchronverter-connected System in Fig. 1

$R_s = 0.741\ \Omega$, $L_s = 20$ mH, $R_e = 0.0\ \Omega$, $L_e = 38.5$ mH, $S_1 = 1$, $S_2 = 0$, $\tau_f = 0.01$ s, $J_g = 2.814\ \mathrm{kg\cdot m^2}$, $D_q = 0\ \mathrm{Var/V}$, $K_g = 27980\ \mathrm{Var\cdot rad/V}$, $\omega_N = \omega^{\star}_g = 376.99\ \mathrm{rad/s}$, $U_\infty = 6.6$ kV, $u_{dc} = 13$ kV, rated grid frequency is 60 Hz, rated ac side voltage is 6.6 kV, and rated synchronverter capacity is 1 MVA.

### B. Proof of Proposed $\gamma$-Criterion via Root Locus Analysis

*1) Start and end points:* The root loci of (22) have three branches. They start from the open-loop poles of $G(s)$ in (23), i.e., the three roots of the equation

$$s^3 + bs^2 + d = 0. \tag{40}$$

One branch ends at $z_1 = 0$, and the other two branches end at $\infty$. We notice that since $b > 0$ and $d > 0$, the discriminant $\Delta_1$ of the third-order polynomial in (40) is [27]

$$\Delta_1 = -4b^3 d - 27d^2 < 0. \tag{41}$$

Thus, (40) has one real root, denoted by $p_1$, and a pair of complex-conjugate poles, denoted by $p_2$ and $p_3$ ($p_2 p_3 \in \mathbb{R}$ and $p_2 p_3 \geq 0$). According to Vieta's formulas [22],

$$-b = p_1 + p_2 + p_3, \tag{42}$$

$$0 = p_1 p_2 + p_2 p_3 + p_1 p_3, \tag{43}$$

$$-d = p_1 p_2 p_3. \tag{44}$$

From (44), $p_1 = -d/(p_2 p_3) < 0$, and from (43), $\mathrm{Re}(p_2) = \mathrm{Re}(p_3) = (p_2 + p_3)/2 = -(p_2 p_3)/(2p_1) > 0$. Thus, $p_1$ is a negative real root, and the real parts of $p_2$ and $p_3$ are both positive. Note that the two branches starting from $p_2$ and $p_3$ provide good approximations for the trajectories of $\lambda_2$ and $\lambda_3$ obtained from (11).

*2) Asymptotes of the root loci:* Two of the branches are asymptotic to the lines emanating from the point $\sigma_a = (p_1 + p_2 + p_3 - z_1)/2 = -b/2$, with angles $\varphi_a = \pm\pi/2$.

*3) Root locus segments on the real axis:* The interval $(p_1, 0)$ is part of the root loci, since there is an odd number of poles and zeros, i.e., $p_2$, $p_3$, and $z_1$ to its right side in the $s$-plane.

*4) Angles of departure/arrival:* Denote angles of departure from poles $p_1$, $p_2$, and $p_3$ as $\theta_{p1}$, $\theta_{p2}$, and $\theta_{p3}$, respectively, then by applying the angle criterion, we have $\theta_{p_1} = 0$, $\theta_{p2} \in (\pi/2, \pi)$, and $\theta_{p3} \in (-\pi, -\pi/2)$. Further denote the angle of arrival at the zero $z_1$ as $\varphi_{z1}$, we get $\varphi_{z1} = \pi$.

*5) Intersection of the root loci with the imaginary axis:* By substituting $s = j\omega$ into (21), and solving it for $\omega$ and $K$, we know that the root loci of (22) intersects the imaginary axis at $s = j\omega = \pm j\sqrt{d/b}$ when $K = d/b$.

*6) Breakaway points:* These are determined by finding the roots of $\frac{dK}{ds} = 0$, which boils down to

$$2s^3 + bs^2 - d = 0. \tag{45}$$

The roots of (45) are denoted by, respectively, $\delta_1$, $\delta_2$, and $\delta_3$ with assumption that $\mathrm{Re}(\delta_1) \leq \mathrm{Re}(\delta_2) \leq \mathrm{Re}(\delta_3)$. Define (which is equivalent to (24))

$$\gamma := b/\left(3\sqrt[3]{d}\right), \tag{46}$$

then the discriminant $\Delta_2$ of (45) is [27]

$$\Delta_2 = 4b^3 d - 108d^2 = 108d^2\left(\gamma^3 - 1\right), \tag{47}$$

and the sign of $\Delta_2$ is determined by the relationship between $\gamma$ and 1. If $\gamma > 1$, then $\Delta_2 > 0$, and (45) has three distinct real roots $\delta_1$, $\delta_2$, and $\delta_3$ ($\delta_1 < \delta_2 < \delta_3$). In this case, we can further show that $p_1 < \delta_1 < \delta_2 < 0 < \delta_3$, i.e., (45) has two negative real roots $\delta_1$ and $\delta_2$ in the range $(p_1, 0)$, and one positive real root $\delta_3 \notin (p_1, 0)$. Since only the interval $(p_1, 0)$ is part of the root loci on the real axis, the root loci of (22) have two distinct breakaway points $\delta_1$ and $\delta_2$. If $\gamma = 1$, then $\Delta_2 = 0$, and (45) has a pair of repeated roots and a real root. In this case, we can further show that $p_1 < \delta_1 = \delta_2 < 0 < \delta_3$, i.e., (45) has repeated negative roots $\delta_1$ and $\delta_2$ in the range $(p_1, 0)$, and a positive real root $\delta_3 \notin (p_1, 0)$. Since only the interval $(p_1, 0)$ is part of the root loci on the real axis, the root loci of (22) have one breakaway point $\delta_1 = \delta_2$. If $0 < \gamma < 1$, then $\Delta_2 < 0$, and (45) has a pair of complex conjugate roots and a real root. In this case, we can further show that $\mathrm{Re}(\delta_1) = \mathrm{Re}(\delta_2) < 0 < \delta_3$, i.e., $\delta_3 \notin (p_1, 0)$, and thus the root loci of (22) have

no breakaway points. With this we complete the proof of the proposed $\gamma$-criterion in (24).

### C. Parameters of Components in Six-bus Test System in Fig. 7

Generators SG1 and SG2: $x_d = 1.56$ p.u., $x_q = 1.06$ p.u., $x'_d = x'_q = 0.296$ p.u., $x''_d = x''_q = 0.177$ p.u., inertia constant $H_{sg} = 8.00$ or $3.00$ s, $T'_{d0} = 3.70$ s, $T'_{q0} = 0.500$ s, $T''_{d0} = T''_{q0} = 0.0500$ s, their rated frequency is 60 Hz, their rated voltage is 6.6 kV, and their rated capacity is 5 MW.

Modified Woodward governor (see Fig. 10) used in SG1 and SG2: $\omega^\star_{sg} = 1.00$ p.u., $P^\star_{sg} = 1.00$ p.u., $K_w = 40.0$ p.u., $R_w = 0.0100$ p.u., $T_{max} = 1.10$ p.u., $T_{min} = 0.00$ p.u., $T_1 = 0.0100$ s, $T_2 = 0.0200$ s, $T_3 = 0.200$ s, $T_4 = 0.250$ s, $T_5 = 0.00900$ s, $T_6 = 0.0384$ s, and $T_d = 0.0240$ s.

Excitation system (see Fig. 11) used in SG1 and SG2: $U^\star_{sg} = 1.03$ p.u., $K_A = 140$, $T_A = 0.0500$ s, $E^{max}_{fd} = 6.00$ p.u., and $E^{min}_{fd} = 0.00$ p.u.

Synchronverter: $R_s$, $L_s$, $S_1$, $S_2$, $\tau_f$, $D_q$, $K_g$, $\omega_N$, $\omega^\star_g$, $u_{dc}$, rated ac side voltage and rated capacity are the same as those in Appendix A, $D_p = 0\ \mathrm{N \cdot m \cdot s/rad}$, $J_g = 21.3$ or $129\ \mathrm{kg \cdot m^2}$, and $D_f = 0.953$ or $2.26\ \mathrm{V \cdot s^2/rad}$.

Transformers T1, T2, and T3: turns ratio is $6.60/13.8$ kV, rated frequency is 60 Hz, leakage reactance is 0.100 p.u., and rated capacities are, respectively, 1.5 MVA, 6.00 MVA, and 6.00 MVA.

Lines Line45, Line46, and Line56: rated frequency is 60 Hz, rated voltage is 13.8 kV, and impedances are, respectively, $0.150 + j1.47\ \Omega$, $0.100 + j1.980\ \Omega$, and $0.100 + j0.980\ \Omega$.

Constant-impedance loads Load1, Load2, and Load3: rated frequency is 60 Hz, rated voltage is 13.8 kV, and impedances are, respectively, $61.0 + j12.2\ \Omega$, $61.0 + j12.2\ \Omega$, and $46.9 + j5.86\ \Omega$.

## ACKNOWLEDGEMENTS

The authors would like to thank Professor Ryozo Nagamune at The University of British Columbia for insightful and helpful discussions on root locus analysis.

## REFERENCES

[1] G. Delille, B. Francois, and G. Malarange, "Dynamic frequency control support by energy storage to reduce the impact of wind and solar generation on isolated power system's inertia," *IEEE Trans. Sustain. Energy*, vol. 3, no. 4, pp. 931–939, Oct. 2012.

[2] Q.-C. Zhong and G. Weiss, "Synchronverters: Inverters that mimic synchronous generators," *IEEE Trans. Ind. Electron.*, vol. 58, no. 4, pp. 1259–1267, Apr. 2011.

[3] H. Wu, X. Ruan, D. Yang, X. Chen, W. Zhao, Z. Lv, and Q.-C. Zhong, "Small-signal modeling and parameters design for virtual synchronous generators," *IEEE Trans. Ind. Electron.*, vol. 63, no. 7, pp. 4292–4303, Jul. 2016.

[4] W. Zhang, A. Cantarellas, J. Rocabert, A. Luna, and P. Rodriguez, "Synchronous power controller with flexible droop characteristics for renewable power generation systems," *IEEE Trans. Sustain. Energy*, vol. 7, no. 4, pp. 1572–1582, Oct. 2016.

[5] Y. Du, J. M. Guerrero, L. Chang, J. Su, and M. Mao, "Modeling, analysis, and design of a frequency-droop-based virtual synchronous generator for microgrid applications," in *Proc. IEEE ECCE Asia Downunder*, 2013, pp. 643–649.

[6] S. Dong and Y. C. Chen, "Adjusting synchronverter dynamic response speed via damping correction loop," *IEEE Trans. Energy Convers.*, vol. 32, no. 2, pp. 608–619, Jun. 2017.

[7] M. Ashabani and Y.-R. Mohamed, "Novel comprehensive control framework for incorporating VSCs to smart power grids using bidirectional synchronous-VSC," *IEEE Trans. Power Syst.*, vol. 29, no. 2, pp. 943–957, Mar. 2014.

[8] F. Gao and M. R. Iravani, "A control strategy for a distributed generation unit in grid-connected and autonomous modes of operation," *IEEE Trans. Power Del.*, vol. 23, no. 2, pp. 850–859, Apr. 2008.

[9] S. D'Arco, J. A. Suul, and O. B. Fosso, "Automatic tuning of cascaded controllers for power converters using eigenvalue parametric sensitivities," *IEEE Trans. Ind. Applicat.*, vol. 51, no. 2, pp. 1743–1753, Mar. 2015.

[10] R. Aouini, B. Marinescu, K. B. Kilani, and M. Elleuch, "Synchronverter-based emulation and control of hvdc transmission," *IEEE Trans. Power Syst.*, vol. 31, no. 1, pp. 278–286, Jan. 2016.

[11] T. Shintai, Y. Miura, and T. Ise, "Oscillation damping of a distributed generator using a virtual synchronous generator," *IEEE Trans. Power Del.*, vol. 29, no. 2, pp. 668–676, Apr. 2014.

[12] M. A. Torres, L. A. C. Lopes, L. A. Moran, and J. R. Espinoza, "Self-tuning virtual synchronous machine: A control strategy for energy storage systems to support dynamic frequency control," *IEEE Trans. Energy Convers.*, vol. 29, no. 4, pp. 833–840, Dec. 2014.

[13] D. Li, Q. Zhu, and S. Lin, "A self-adaptive inertia and damping combination control of vsg to support frequency stability," *IEEE Trans. Energy Convers.*, vol. 32, no. 1, pp. 397–398, Mar. 2017.

[14] H. P. Beck and R. Hesse, "Virtual synchronous machine," in *Proc. 9th Int. Conf. EPQU*, 2007, pp. 1–6.

[15] N. Soni, S. Doolla, and M. C. Chandorkar, "Improvement of transient response in microgrids using virtual inertia," *IEEE Trans. Power Del.*, vol. 28, no. 3, pp. 1830–1838, Jul. 2013.

[16] S. Wang, J. Hu, and X. Yuan, "Virtual synchronous control for grid-connected DFIG-based wind turbines," *IEEE J. Emerg. Sel. Topics Power Electron.*, vol. 3, no. 4, pp. 932–944, Dec. 2015.

[17] C. Li, J. Xu, and C. Zhao, "A coherency-based equivalence method for MMC inverters using virtual synchronous generator control," *IEEE Trans Power Del.*, vol. 31, no. 3, pp. 1369–1378, Jun. 2016.

[18] D. Dong, B. Wen, D. Boroyevich, P. Mattavelli, and Y. Xue, "Analysis of phase-locked loop low-frequency stability in three-phase grid-connected power converters considering impedance interactions," *IEEE Trans. Ind. Electron.*, vol. 62, no. 1, pp. 310–321, Jan. 2015.

[19] P. Kundur, N. J. Balu, and M. G. Lauby, *Power system stability and control*. New York: McGraw-hill, 1994.

[20] J. M. Guerrero, L. G. de Vicuna, J. Matas, M. Castilla, and J. Miret, "A wireless controller to enhance dynamic performance of parallel inverters in distributed generation systems," *IEEE Trans. Power Electron.*, vol. 19, no. 5, pp. 1205–1213, Sep. 2004.

[21] F. Golnaraghi and B. Kuo, *Automatic Control Systems*, 9th ed. New York: Wiley, 2010.

[22] J. W. Harris and H. Stöcker, *Handbook of Mathematics and Computational Science*. New York: Springer-Verlag, 1998.

[23] R. A. Horn and C. R. Johnson, *Matrix analysis*. Cambridge, U.K.: Cambridge Univ. Press, 2012.

[24] G. Berg and A. Ghafurian, "Representation of coherency-based equivalents in transient stability studies," *Electric Power Syst. Res.*, vol. 6, no. 4, pp. 235–241, Dec. 1983.

[25] K. E. Yeager and J. R. Willis, "Modeling of emergency diesel generators in an 800 megawatt nuclear power plant," *IEEE Trans. Energy Convers.*, vol. 8, no. 3, pp. 433–441, Sep. 1993.

[26] P. Sauer and M. Pai, *Power System Dynamics and Stability*. N.J.: Prentice Hall, 1998.

[27] J. L. Awange and E. W. Grafarend, *Solving Algebraic Computational Problems in Geodesy and Geoinformatics*. Berlin: Springer-Verlag, 2005.

[28] E. P. Popov, *The Dynamics of Automatic Control Systems*. Elsevier, 1962.